Acta Materialia 304 (2026) 121749

Contents lists available at ScienceDirect

Acta Materialia

journal homepage: www.elsevier.com/locate/actamat

Capacitive energy-storage and electromechanical properties of aerosol-deposited $0.5BaZr_{0.2}Ti_{0.8}O_3$–$0.5Ba_{0.7}Ca_{0.3}TiO_3$ films

Soukaina Merselmiz [a,†], Ivana Goričan [a,b,†], Tadej Rojac [a,b], Vid Bobnar [b,c], Victor Regis [a,b], Matej Šadl [a], Val Fišinger [a], Nejc Suban [a,b], Brigita Kmet [a], Andreja Benčan [a,b], Andraž Bradeško [a], Andrej Debevec [a], Barbara Malič [a,b], Hana Uršič [a,b,*]

[a] Electronic Ceramics Department, Jožef Stefan Institute, Jamova cesta 39, 1000 Ljubljana, Slovenia
[b] Jožef Stefan International Postgraduate School, Jamova cesta 39, 1000 Ljubljana, Slovenia
[c] Department of Condensed Matter Physics, Jožef Stefan Institute, Jamova cesta 39, 1000 Ljubljana, Slovenia

ARTICLE INFO

Keywords:
Powder aerosol deposition
Ceramics
Thick films
Ferroelectricity
Piezoelectricity

ABSTRACT

Integrating functional ceramic thick films onto metal substrates for advanced electronic applications is challenging due to the high sintering temperatures. To address this issue, low-temperature processing methods such as aerosol deposition (AD) offer an effective solution. In this study, lead-free $0.5Ba(Zr_{0.2}Ti_{0.8})O_3$–$0.5(Ba_{0.7}Ca_{0.3})TiO_3$ (BZT–BCT) thick films were prepared on low-cost stainless-steel substrates using the AD method. The as-deposited films exhibited a dense microstructure and excellent adhesion to the substrate. After deposition, the films were annealed at 500 °C and 800 °C. The films annealed at 800 °C demonstrated enhanced ferroelectric behavior compared to both the as-deposited films and those annealed at 500 °C. These films also exhibit a high dielectric breakdown strength exceeding 1400 $kV{\cdot}cm^{-1}$, making them promising for energy storage applications. The recovered energy density and energy efficiency reach 9.5 $J{\cdot}cm^{-3}$ and 84 %, respectively, at 1500 $kV{\cdot}cm^{-1}$. Moreover, the recovered energy density demonstrated excellent electric-field cycling stability up to 100 million cycles, as well as thermal stability from −50 °C to 200 °C at 400 $kV{\cdot}cm^{-1}$. The field-induced strain response of the films annealed at 800 °C demonstrated an electromechanical performance with a maximum strain of 0.05 % at 350 $kV{\cdot}cm^{-1}$, corresponding to a converse effective piezoelectric coefficient of 15.5 $pm{\cdot}V^{-1}$. The dominating factor for such a relatively low value is most likely the fine microstructure. Overall, the results highlight the potential of integrating lead-free ceramic films onto low-cost stainless-steel substrates to form functional structures, especially for energy storage applications, where good thermal and electrical cycling stability is essential.

1. Introduction

Piezoceramics such as $Pb(Zr,Ti)O_3$ (PZT) dominate in microelectronics, medical diagnostics, sensors and actuators devices. However, due to the high toxicity of lead and increasing restrictions on lead-containing materials by the European Union, Japan, and the United States, research has focused on developing lead-free alternatives with similar piezoelectric properties [1–3]. The $(1–x)BaZr_{0.2}Ti_{0.8}O_3$–$xBa_{0.7}Ca_{0.3}TiO_3$ morphotropic phase boundary composition, where $x = 0.5$ (in the further text noted as BZT–BCT) is reported to be one of the best lead-free piezoelectric materials, achieving a piezoelectric coefficient (d_{33}) of up to ~600 $pC{\cdot}N^{-1}$ [4–9]. Such high piezoelectric performance was first attributed to the morphotropic phase boundary (MPB) between the rhombohedral and tetragonal phases. Later, an intermediate orthorhombic phase between the rhombohedral and tetragonal phases was identified in the phase diagram of the BZT–BCT system [10]. The high piezoelectric performance was then ascribed to the MPB between the orthorhombic and tetragonal phases [11].

Furthermore, ceramics with the promise for capacitive storage applications are of high interest. Dielectric capacitors store and release energy through charge displacement stimulated by an external electric field, resulting in high power density, excellent stability, and ultrafast charge/discharge performance, which are crucial for pulsed-power applications [12,13]. In general, the energy storage performance of

* Corresponding author at: Electronic Ceramics Department, Jožef Stefan Institute, Jamova cesta 39, 1000 Ljubljana, Slovenia.
E-mail address: hana.ursic@ijs.si (H. Uršič).
† The authors contributed equally to this work.

https://doi.org/10.1016/j.actamat.2025.121749
Received 1 July 2025; Received in revised form 24 October 2025; Accepted 19 November 2025
Available online 20 November 2025

dielectric capacitors is deduced from the recovered storage density (U_{rec}) and energy storage efficiency (η), which require high saturated polarization (P_s), low remanent polarization (P_r), low energy loss density (U_{loss}), and high dielectric breakdown strength (DBS) [14]. So far, a wide scientific community has been focuced on the preparation of materials for energy storage, and ceramic materials with extremely large U_{rec} values (> 10 J·cm^{-3}) have been developed [15–22]. The aforementioned BZT–BCT-based compositions have also been reported to be promising to store energy, especially when prepared as thin films (U_{rec} values > 45 J·cm^{-3}) [23–25].

In comparison with thin film technologies, where films are prepared from solutions [26,27], thick film technologies are based on powders [28–30]. Nevertheless, the integration of ceramic thick films on low-melting-point substrates remains challenging due to conventional deposition methods, such as screen printing [31], which require high temperatures, often exceeding 1000 °C. These high temperatures are crucial for densifying ceramic thick films and for achieving strong adhesion to the substrates. However, this requirement hinders the integration of ceramics with temperature-sensitive materials such as polymers, metals and alloys.

To address the integration challenge, the aerosol deposition (AD) method, a room-temperature spray-coating technique, can serve as an innovative solution. This deposition method produces highly dense films (>95 %) with thicknesses up to several hundred micrometers on various substrates [32,33]. The AD method outperform conventional film deposition routes in processing time and cost. It allows the integration of ceramic films on low-melting point substrates such as, metals, glasses, or polymers [32,34–39]. In AD, the powder is mixed with a carrier gas to form an aerosol, which is then accelerated through a nozzle into the deposition chamber. The particles collide with the substrate surface, break, and form a film [32,33]. During this process, stresses are formed in the direction of particle movement (vertical direction within the films). These stresses are found to be in the range of MPa–GPa [40–42] and can hinder the functional properties of the films. The stresses can be reduced by thermal treatment, usually at a few hundred degrees [34,40, 42]. Such annealing results in lower internal residual stresses, an increase in crystallinity, pore redistribution and grain growth compared to as-deposited films [34,35,42–48].

For energy applications, the integration of metals and their alloys as substrates for functional thick films is highly advantageous due to their excellent electrical conductivity and mechanical stability [34,49]. Stainless steel (SS), in particular, is a durable, corrosion and wear-resistant metal. It is also cost-effective and easily accessible. It is of great importance for buildings, power stations, medicine, vehicles, space crafts, etc. [50–53]. Functional thick films prepared on stainless-steel substrates would open up significant opportunities for use in these fields. For example, integrating electronic structures directly to the buildings, bridges, railways, trains, space shuttles, or medical devices would be possible if we were able to develop functional electronics on stainless steel. Aerosol deposition is a suitable method for this purpose, as ceramic powders could be directly integrated into various stainless-steel surfaces in the future. For these reasons, stainless steel is also one of the standard materials used for aerosol deposition of a variety of materials [40,54–59], including $BaTiO_3$ (BT)-based materials.

BT films exhibit a piezoelectric coefficient d_{31} within the range from -40 pm·V^{-1} to -56 pm·V^{-1} [55,60] and energy storage properties, namely U_{rec} of 6.8 J·cm^{-3} with an η of 83 % at 1 MV·cm^{-1} [61]. Meanwhile, it was reported that annealing of aerosol-deposited BT thick films on SS substrates at 750 °C improves the dielectric properties by promoting grain growth [62]. Furthermore, in the literature two reports can be found on aerosol-deposited BZT–BCT thick films on SS substrates [59,63]. In the first one, the authors prepared 11-μm-thick BZT–BCT films on SS substrates and annealed them at 600 °C. In the second report, 80-μm-thick BZT–BCT films were prepared on SS substrates and annealed at 500 °C. The polarization versus electric field measurements showed an almost linear dielectric response in both cases. Furthermore, the films in ref. [63] exhibited no piezoelectric response, and no piezoelectric measurements were reported in ref. [59]. In addition, free-standing BZT–BCT thick films were prepared and annealed at higher temperatures. The films, annealed at 1000 °C, showed a potential for energy storage capacitors, since the U_{rec} and η of 1.34 J·cm^{-3} and 82 %, respectively at 200 kV·cm^{-1} were determined [59]. In summary, annealing the BZT–BCT films at 500 °C and 600 °C resulted in poor functional properties, while annealing at 1000 °C improved the energy storage properties, suggesting that the annealing temperature plays an important role in the development of good functional properties for BZT–BCT thick films.

In this study, BZT–BCT thick films were deposited on stainless steel substrates using the AD method. The composition was chosen due to the previously mentioned promise of multifunctionality. After deposition, the films were annealed at 500 °C to allow comparison with the literature and also at 800 °C to improve the functional properties. The structural, microstructural, dielectric, ferroelectric and electromechanical properties of the as-deposited and annealed thick films were investigated. The BZT–BCT thick films annealed at 800 °C exhibited a significantly enhanced ferroelectric response compared to both the as-deposited films and those annealed at 500 °C. Consequently, our research focused on the energy storage and electromechanical properties of the thick films annealed at 800 °C. The films exhibited multifunctional behaviour, highlighting their potential for use in future electronic applications.

2. Experimental procedure

$0.5BaZr_{0.2}Ti_{0.8}O_3$–$0.5Ba_{0.7}Ca_{0.3}TiO_3$ (abbreviated BZT–BCT) ceramic powder was prepared by the conventional solid-state method using $BaCO_3$ (99.8 %, Alfa Aesar, Karlsruhe, Germany), $CaCO_3$ (99.95 %, Alfa Aesar, Karlsruhe, Germany), TiO_2 (99.8 %, Alfa Aesar, Karlsruhe, Germany) and ZrO_2 (99.8 %, Tosoh, Japan) as starting powders. $BaCO_3$, $CaCO_3$, ZrO_2 and TiO_2 were stoichiometrically weighed, mixed and homogenized using isopropanol, in a planetary mill (PM 400, Retsch) with yttria-stabilized zirconia milling bodies (3 mm, Tosoh, Japan) for 1 h at 200 rpm. The homogenized powder was then dried at 110 °C and sieved. The BZT–BCT powder mixture was calcined at 1300 °C for 4 h in the air with heating and cooling rates of 5 K·min^{-1}. The calcined powder was wet-milled in isopropanol using a planetary mill for 1 h at 200 rpm, dried at 120 °C and sieved. The prepared batch of BZT–BCT weighed 100 g.

Particle size analysis was performed using a light-scattering laser granulometer (S3500, Microtrac, USA) with isopropanol as the medium. Prior to the measurement, the powder suspended in the liquid medium was placed in an ultrasonic bath (PRO 50, ASonic, China) for a few minutes to break up the agglomerates. A powder with a particle size in the range of a few hundred nanometres to micrometres was used for the preparation of thick films by AD process. The d_{50} and d_{90} values of the used powder were determined to be 0.68 μm and 2.75 μm, respectively. The particle size distribution is shown in Supplementary material S1.

Prior to the deposition, the powder was sieved through an 80-μm mesh and vacuum dried at 100 °C for 12 h and at 10 mbar. The prepared powder was deposited onto a commercial stainless-steel substrate (SS, no. 304, American Iron and Steel Institute, USA) with a bright, polished surface (A480: No. 8, American Society for Testing and Materials) and dimensions of 15 mm × 15 mm × 0.8 mm. 10 g of the BZT–BCT powder were used to prepare ten thick-film samples. The AD equipment was provided by InVerTec, Germany, and it is schematically shown in ref. [64]. The process parameters during AD are presented in Supplementary material S2. After deposition, the obtained thick films were cleaned with ethanol and annealed at different temperatures in order to release the internal stresses developed in the material during deposition. The as-deposited films will be further referred to as “ADep” films. The films were then annealed at 500 °C for 1 h (further referred to as “PA-500″), followed by annealing at 800 °C for 2 h (further referred to as “PA-800”).

The heating and cooling rates of 5 K·min^{-1} were used.

The X-ray diffraction (XRD) patterns of the samples were measured with a high-resolution diffractometer (X'Pert PRO, PANalytical, Netherlands) with Cu–Kα_1 radiation. Diffraction patterns were recorded over the 2θ-range 10–90° with a step size of 0.017° and an integration time of 100 s per step. The phase structure of BZT–BCT was determined on a powder sample using FullProf Suite (version 7.95, Institute Laue-Langevin, France) through the Rietveld refinement approach [65], which is presented in Supplementary material S3. The crystallite size and microstrain were determined using the Williamson-Hall method based on the Full Width at Half Maximum (FWHM) of the XRD peaks [66,67].

The microstructures of the powder and thick films were analyzed using a field-emission scanning electron microscope (FE-SEM, JSM-7600F, JEOL, Japan) equipped with a backscattered electron (BE) detector and an energy-dispersive X-ray spectrometer (EDXS, Inca Oxford 350 EDS SSD, Oxford Instruments, UK). The EDXS spectra were acquired at 10 keV. In order to analyze the cross-section of the thick films, the samples were cut, embedded in epoxy resin, ground, polished with diamond paste and fine-polished using a colloidal SiO_2 suspension. Prior to the SEM analysis, a 3 nm-thick carbon coating was deposited on the samples using a Precision Etching and Coating System (PECS 682, Gatan, USA). The images were acquired using an accelerating voltage of 15.00 kV, an emission current of ~73 μA and a tilting angle of 0 °. The thickness of the thick films was evaluated from SEM cross-sectional images and was found to be ~ 6 μm. The cross-sectional EDXS analysis of the PA-500 films are presented in Supplementary material S4.

Atomic force microscopy (AFM) was used to determine the surface roughness (R_q) of the films. Details of the measurements and results can be found in Supplementary material S5. Furthermore, an AFM and piezo-response force microscopy (PFM) analyses were performed on as-deposited and annealed thick films at the polished cross-sectional surface, as described in ref. [68]. An atomic force microscope (MFP-3D, Asylum Research, USA) and Ti/Ir coated silicon tips (Asyelec 01 R2, Oxford Instruments, Germany) were used for recording the topography (height image, contact mode) and PFM images. To examine the samples in the cross-section, electric voltages of 2–5 V, and frequencies of approximately 300–360 kHz were applied in the virtual ground regime, as previously described in ref. [68]. After the PFM scans, the PFM phase hysteresis loops were measured by switching spectroscopy with the pulsed DC step signal and the superimposed AC drive signal, as described in ref. [69]. The waveform parameters were driven at 20 Hz and a maximum amplitude of 30 V; the frequency of the triangular envelope was 0.99 Hz; a superimposed sinusoidal AC signal with an amplitude of 3 V and a frequency of ~ 330 kHz was used. Three cycles were measured in an off-electric-field mode.

For the macroscopic electrical measurements, the SS substrate acted as a bottom electrode, while the top Au electrodes of a diameter of 0.5 mm were deposited by RF-magnetron sputtering machine (5 Pascal, Trezzano sul Naviglio, Italy). The relative dielectric permittivity (ε_r) and dielectric loss ($tan\ \delta$) as a function of temperature were analyzed during cooling from 200 °C to 0 °C using an aixACCT TF analyzer 2000 (aixACCT Systems GmbH, Aachen, Germany) coupled with a HP 4284A Precision LCR impedance meter (Hewlett-Packard, California, USA). The measurements were performed in a frequency range of 0.1–10 kHz for ADep and PA-500 films and in a frequency range of 0.1–100 kHz for PA-800 samples. The frequency dispersion of the peak-permittivity temperatures was analyzed as discussed in Supplementary material S6.

Polarization–electric field (*P–E*) hysteresis loops were recorded using an aixACCT TF analyzer 2000 by applying a bipolar single sinusoidal waveform with an amplitude of up to 1.4 MV·cm^{-1} and a frequency of 100 Hz at room temperature (RT). In order to determine the electric field dependence of the energy storage properties for the PA-800 sample, three consecutive unipolar *E* cycles of the hysteresis loops (*P–E*) were measured using sinusoidal waveforms with an amplitude of 1.5 MV·cm^{-1} and a frequency of 100 Hz at RT. The second *E* cycle was then used for the calculations of energy storage performance as explained in Supplementary material S7. Furthermore, temperature-dependence of the unipolar hysteresis *P–E* loops was measured from 200 °C to −50 °C, using unipolar sinusoidal-like waveforms with an amplitude of 400 kV·cm^{-1} and a frequency of 100 Hz. The energy storage properties were calculated as explained above.

Fatigue measurements were performed by applying to the sample a total of 100 million unipolar sinusoidal-like field cycles with a frequency of 1 kHz and an amplitude of 400 kV·cm^{-1}. Within each decade of fatigue pulses, 3 monitoring measurements were performed to determine the energy storage properties. In the monitoring measurements, two consecutive unipolar *E* cycles of the hysteresis loops (*P–E*) were measured, and the second *E* cycle was used for the calculations of energy storage performance. For these measurements, a frequency of 50 Hz and an electric field amplitude of 400 kV·cm^{-1} was used. Furthermore, the fatigue measurements were performed at 750 kV·cm^{-1}, and the results are presented in Supplementary material S8.

The DBS measurements were investigated using an aixACCT TF analyzer 2000 by using the Breakdown Measurement mode. The Weibull distribution was used for the determination of the DBS, as presented in Supplementary material S9.

Furthermore, RT strain–electric field (*S–E*) hysteresis loops were measured with Au electrodes of size 1 mm x 2 mm using an aixACCT TF analyzer 2000 equipped with a single-beam laser interferometer. The applied *E* had a triangular waveform with an amplitude of 220, 300 and 350 kV·cm^{-1} and a frequency of 100 Hz. To confirm the results, an aixACCT TF analyzer 2000 equipped with a double-beam laser interferometer was also used. To ensure a flat surface and laser reflection, an SS foil was attached to the part of the Au electrode. For a similar reason, a gold foil was placed below the SS substrate, which acts as the bottom electrode of the sample. The applied *E* had a triangular waveform with an amplitude of 220 kV·cm^{-1} and a frequency of 100 Hz. The comparison of the results obtained with the two instruments is presented in Supplementary material S10.

3. Results and discussions

3.1. Structural and microstructural properties

The structural properties of BZT–BCT powder and as-deposited and annealed thick films were investigated by XRD analysis. In the XRD patterns, peaks corresponding mainly to the perovskite phase are observed (Fig. 1). Minor additional peaks corresponding to the $CaTiO_3$ secondary phase are also visible. The phase structure of the BZT–BCT powder was analyzed using Rietveld refinement, as shown in Fig. S3 of Supplementary material S3. The best fit was obtained with 85 % of the orthorhombic *Amm*2 symmetry and 15 % of the tetragonal *P4mm* symmetry. The coexistence of these two phases was previously reported for BZT–BCT [70]. The agreement factors of the Rietveld analysis, along with the cell parameters, are given in Table S3 in Supplementary material S3. In the XRD patterns of the films, the additional peaks marked as SS peaks are attributed to the SS substrate. The XRD pattern of the PA-800 film exhibits minor peaks (marked with a plus sign), most probably due to the reaction of the film with the substrate. The peak positions closely resemble those of the $BaCrO_4$ compound (PDF 04–020–6542 [71]), which will be discussed in more detail later in correlation with the EDXS analysis.

As the particles, which may be monocrystalline or polycrystalline, break during the aerosol deposition process, the crystallites inside the particles also fracture. However, the crystallite size can increase if the samples are annealed [37]. As the annealing temperature increases, the crystallinity of the samples improves as indicated by the perovskite peaks in the XRD patterns (Fig. 1a), which become narrower. Furthermore, annealing the samples reduces the stresses in the aerosol-deposited films [34,42], which is reflected by a decrease in microstrain. The influence of annealing temperature on crystallite size

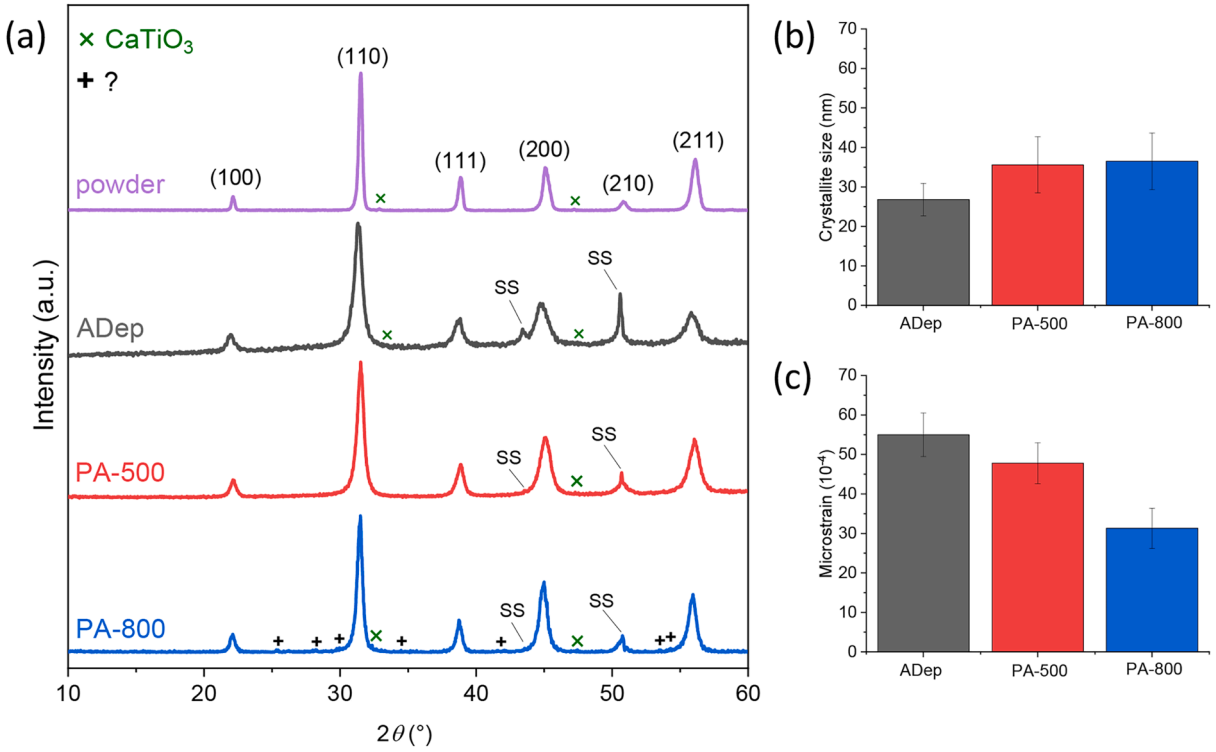

Fig. 1. (a) XRD diffraction patterns for BZT–BCT powder, ADep, PA-500 and PA-800 films. For the convenience of visualization, the diffraction peaks were indexed using the pseudocubic setting according to the space group *Pm3m* (PDF 01–074–4539 [74]). The diffraction peaks marked by multiplication sign correspond to the $CaTiO_3$ (PDF 01–082–0229 [75]) secondary phase. The additional peaks marked with SS are attributed to the surrounding stainless-steel substrates. The plus sign in the XRD pattern of the PA-800 film indicates the peaks corresponding to the secondary phase due to the reaction between the film and the substrate. The corresponding (b) crystallite size and (c) microstrain were determined by the Williamson-Hall method.

and microstrains was determined using the Williamson-Hall method, as shown in Fig. 1b, c. The obtained values indicate that with increasing annealing temperature, the crystallite size increases from 26.8 nm ± 4.1 nm to 36.5 nm ± 7.2 nm for ADep and PA-800 films, respectively. In addition, the microstrain value decreases for 43 %, namely from $55{\cdot}10^{-4}$ ± $5.5{\cdot}10^{-4}$ to $31.3{\cdot}10^{-4}$ ± $5.1{\cdot}10^{-4}$ for the ADep and PA-800 films, respectively. However, the thermal expansion coefficients (TECs) are ~$12{\cdot}10^{-6}$ K^{-1} [72] and ~$17{\cdot}10^{-6}$ K^{-1} [73] for BZT–BCT and SS, respectively. BZT–BCT has a lower TEC compared to the substrate, which

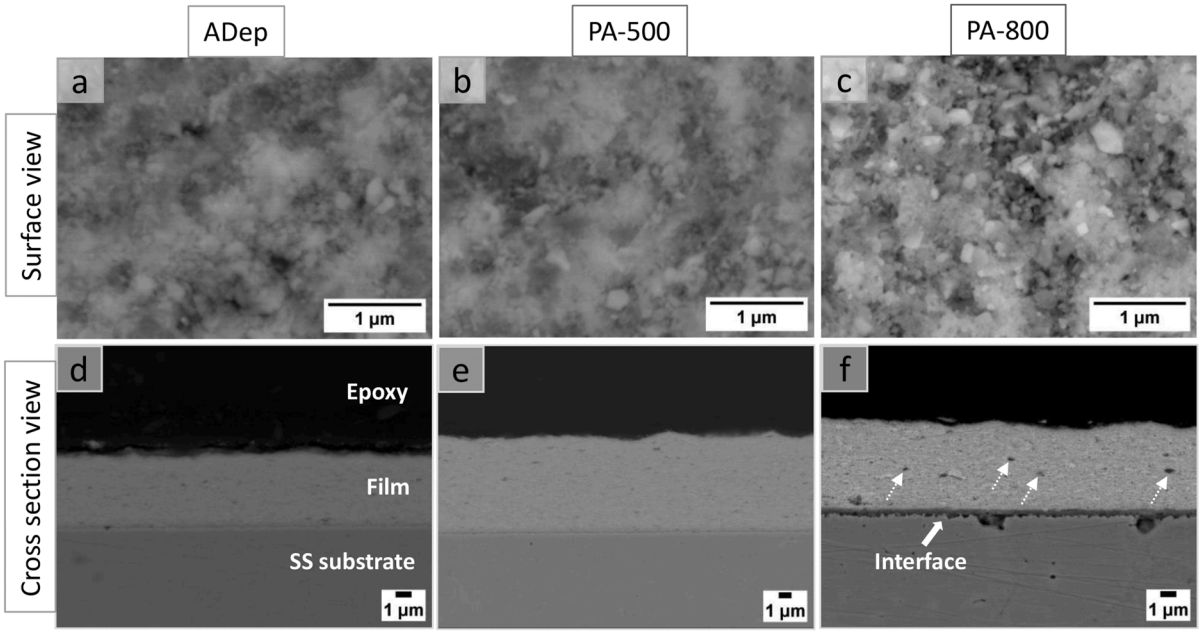

Fig. 2. BE–SEM images of (a, d) the ADep, (b, e) PA-500 and (c, f) PA-800 films in surface (a–c) and cross-sectional (d–f) views. Thick solid arrow in panel (f) marks the interface layer between the stainless-steel substrate and the film. The dark inclusions in panel (f) are pores (marked by thin dashed arrows).

results in compressive stresses [26].

The microstructural properties of the as-deposited and annealed thick films were analyzed by BE–SEM in surface and cross-sectional views (Fig. 2). The surface view of all the samples reveals a typical surface produced by the AD method, characterized by a dense microstructure with nano-sized, powder-like particles scattered across the surface (Fig. 2a–c). Compared to Adep, slight grain growth is observed on the surfaces of the annealed films, especially for the PA-800 film (Fig. 2c). However, the grains in our films remain in the nanometre range even after annealing at 800 °C, making it difficult to determine their average size. Our results are in agreement with the literature [48], where slight grain growth was observed for $Pb(Mg_{1/3}Nb_{2/3})O_3$–$PbTiO_3$ aerosol-deposited samples annealed at 500 °C. Furthermore, the R_q values of the film surfaces were determined and found to be comparable for all films. Details are provided in Supplementary material S5.

In cross-sectional view, both the ADep and PA-500 films exhibit a dense microstructure, excellent adhesion to the substrate, and no visible degradation of either the film or the substrate due to the annealing, as shown in Fig. 2d, e. Similarly, the PA-800 film also exhibits a dense microstructure; however, in this case, a clearly defined film-substrate interface layer with a thickness of ~ 500 nm is observed as shown in Fig. 2f. An additional Ca-rich secondary phase was observed in all films, which is in agreement with the XRD analysis (Fig. 1). The EDXS analysis of this phase is shown in Supplementary material S4. Further comparison of the film cross-sections also reveals that annealing of the films affects a pore distribution, which is in consistent with the literature [48]. In the case of ADep and PA-500 films, the pores are in nano-metre range, while in the PA-800 films, due to pore redistribution, the pores become a bit larger but are still in the range of tens to a hundred nanometres, as shown by the white arrows in Fig. 2f. We cannot exclude the possibility that annealing the samples may also lead to slight densification of the films, particularly in the case of the PA-800 films.

To examine the cross-section of the PA-800 films in more detail, an EDXS line scan was performed from the substrate through the film thickness as shown in Fig. 3a. The resulting concentration profiles for the chemical elements (Ba, Ti, Ca, Zr, Cr, Fe and Ni) are also presented in Fig. 3a. The results indicate the formation of a distinct film-substrate interface layer, mainly rich in chromium and iron, with a minor presence of nickel. These elements, which are alloying components of stainless steel, suggest diffusion into the thick film in regions close to the substrate. These results are supported by a cross-sectional EDXS analysis performed in two locations, namely in the interface layer region (marked by a red cross) as well as in the BZT–BCT matrix (marked by a blue cross), as shown in Fig. 3a. The EDXS spectrum corresponding to the matrix (blue color) shows pronounced peaks corresponding to BZT–BCT composition elements (Ba, Ca, Zr, Ti and O), while the spectrum from the interface layer (red color) also reveals pronounced peaks for stainless-steel alloying elements, especially chromium and iron (Fig. 3b). Please note that the interaction volume of the EDXS analysis is approximately 1 μm in width, while the thickness of the interface layer is around 500 nm.

According to the EDXS analysis, the interface layer contains iron and chromium, in addition to the elements of the BZT–BCT composition. In the XRD pattern of the PA-800 films (Fig. 1), besides the perovskite peaks and the peaks of the $CaTiO_3$ secondary phase, additional peaks marked with (?) can also be observed. These peaks could not be indexed using existing XRD reference cards that cover all the mentioned elements. However, as mentioned previously, their positions closely resemble those of the $BaCrO_4$ compound (PDF 04–020–6542 [71]). This suggests that the additional peaks observed in the XRD diffraction of the PA-800 films are likely associated with the interface layer. The thickness of the films is ~ 6 μm, while calculations in the HighScore Plus program estimate the penetration depth of X-rays in BZT–BCT could be up to 9 μm.

3.2. Local ferroelectric properties

Microstructural features and piezoelectric performance across the film thicknesses were investigated using atomic force microscopy (AFM) with an attached piezo-response force microscopy (PFM) module. The topographic height and deflection AFM images, along with the PFM out-of-plane amplitude images of the as-deposited and annealed thick films in the cross-section, are shown in Fig. 4. All thick films present a dense microstructure, as shown in the topography height (Fig. 4a–c) and deflection (Fig. 4d–f) images, and are piezoelectrically active over their entire thickness (bright regions), as displayed in the PFM out-of-plane amplitude images (Fig. 4g–i). The SS substrates do not exhibit any piezoelectric response, as evidenced by the dark regions in the PFM amplitude images. Similarly, the interface layer in the PA-800 film does not show any piezoelectric performance, as shown in Fig. 4i. It is worth mentioning that the piezoelectric response is enhanced by increasing the annealing temperature of the films, as demonstrated by increased PFM

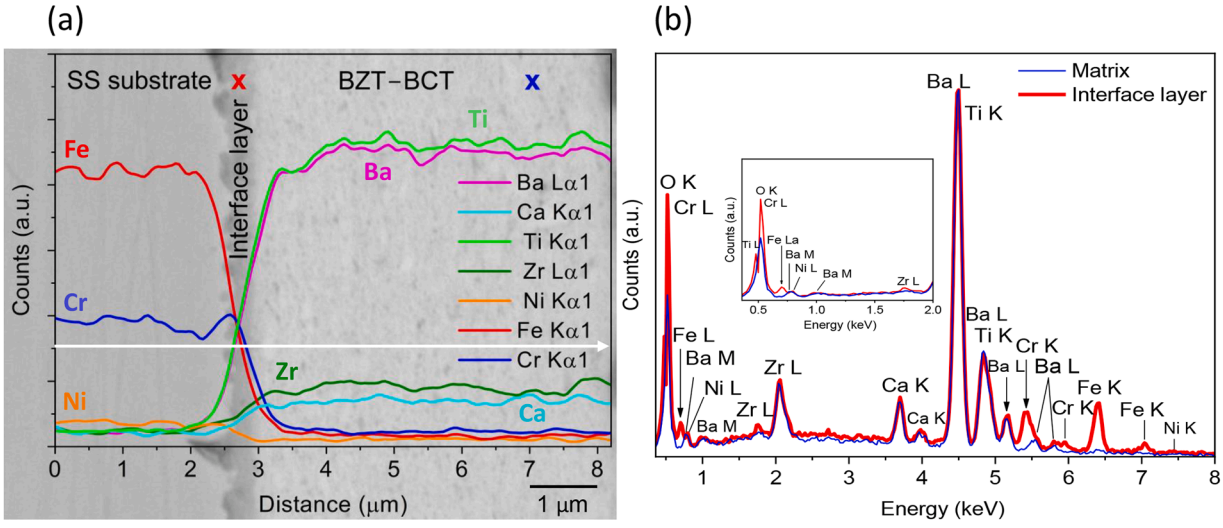

Fig. 3. (a) Cross-sectional BE–SEM image of the PA-800 film, including the EDXS line scan profile along a selected straight line (indicated by the white arrow), showing the variation of Ba, Ti, Ca, Zr, Cr, Fe and Ni elements across the stainless-steel substrate, the interface and the PA-800 film. (b) The corresponding EDXS spectra of the PA-800 films. The crosses in panel (a) mark the matrix phase (BZT–BCT) and interface layer regions. Please note that all peaks were normalized to the highly intense Ba/Ti peak. Additionally, some peaks in the spectra overlap, so multiple elements are indicated near these peaks.

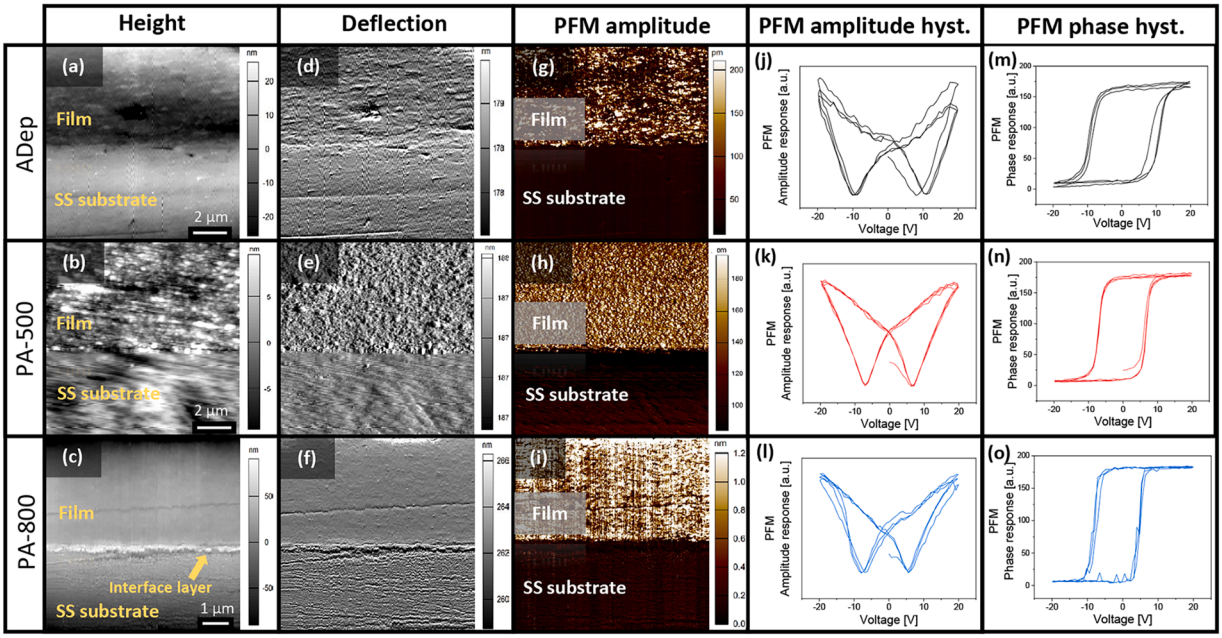

Fig. 4. AFM (a–c) topography height and (d–f) deflection and (g–i) PFM out-of-plane amplitude images of (a, d, g) ADep, (b, e, h) PA-500 and (c, f, i) PA-800 films on stainless-steel substrate in cross-section. The arrow in panel (c) marks the interface layer between the stainless-steel substrate and the PA-800 film. Switching spectroscopy experiment; (j–l) local amplitude and (m–o) phase hysteresis loops.

amplitude and the expanding bright regions within the film cross sections (Fig. 4g–i). Additionally, a PFM local switching spectroscopy experiment was recorded in as-deposited and annealed films, as presented in Fig. 4j–o. These results reveal local PFM amplitude and phase hysteresis loops typical of piezoelectric/ferroelectric materials, indicating effective switching of ferroelectric domains in all films.

3.3. Macroscopic electrical properties

3.3.1. Dielectric properties

The relative dielectric permittivity (ε_r) and the dielectric losses (*tan* δ) of the ADep, PA-500 and PA-800 films are shown in Fig. 5. For the ADep films, the ε_r value at room temperature was found to be ~ 94 at 1 kHz (Fig. 5a), which increases to ~134 after annealing at 500 °C (Fig. 5b). The ADep and PA-500 films exhibit a tan $\delta < 0.05$ at 1 kHz and room temperature. As the temperature increases to 200 °C, the ADep films show an increase in tan δ to ~ 0.35 at 1 kHz, while the PA-500 films show a decrease in tanδ to 0.12 at 1 kHz. The increase in tan δ with rising temperature in both the ADep and PA-500 films could be related to the relaxation of space charges that become mobile at higher temperatures. Similar behaviors has also been observed in other aerosol-deposited thick films [34,61].

Further annealing at 800 °C, results in an increase in ε_r to ~ 562 at 1 kHz and room temperature. These films show a tan $\delta \sim 0.12$ at 1 kHz and room temperature, while the tan δ values maintain < 0.1 at 200 °C at all used frequencies (Fig. 5c). The PA-800 films exhibit broad, frequency-dependent permittivity peaks as a function of temperature, indicating a relaxor-like behavior. The frequency dispersion of the peak-permittivity temperatures was analyzed by evaluating the temperature derivative of the dielectric permittivity. Details can be found in Supplementary material S6. The difference between the peak-permittivity temperature at 0.1 kHz and 100 kHz is determined to be ~ 55 °C. At 1 kHz, the maximum permittivity is 640 at ~ 115 °C, which is ~ 25 °C higher compared to that observed in BZT–BCT bulk ceramics, where the Curie temperature (T_c) between tetragonal and cubic phases occurs at ~ 90 °C at 1 kHz [4,72]. The shift to higher temperatures is presumably related to the above mentioned compressive stresses formed in the samples [76]. Furthermore, in BZT–BCT ceramics, enhanced relaxor behavior is observed in the samples with an average grain size below micrometer [77], which is also the case in prepared aerosol-deposited films [32].

The frequency dispersion at the maximum peak and the broadening of the permittivity peak have been observed in other lead-based and lead-free aerosol-deposited films and are likely attributed to residual stresses formed during aerosol deposition, as well as microstructural differences compared to their bulk ceramic counterparts [34,58,61,78–80].

3.3.2. Ferroelectric properties and energy-storage performance

The ferroelectric properties of the ADep, PA-500 and PA-800 films were studied. Room temperature bipolar polarization–electric field (*P–E*) hysteresis loops measured at 800 kV·cm^{-1} are shown in Fig. 6a. Both the ADep and PA-500 films show a hysteretic dielectric-like behavior. In contrast, the PA-800 films demonstrate ferroelectric properties, exhibiting a larger maximum polarization (P_{max}) compared to the ADep and PA-500 films. Note that the relative dielectric permittivity is also improved by annealing at 800 °C, as shown above in Fig. 5c. Furthermore, during the *P–E* measurements, the 800 °C films withstand the highest electric field of 1.4 MV·cm^{-1} and reach a P_{max} of 28.5 µC·cm^{-2}, as shown in Fig. 6b. These ferroelectric properties are enhanced compared to already published ones for $BaTiO_3$ thick films on SS substrates annealed at 750 °C with a $P_{max} \sim 5.3$ µC·cm^{-2} at 500 kV·cm^{-1} [62]. Since the PA-800 films withstand the highest electric field and exhibit better ferroelectric performance than the ADep and the PA-500 films, we have focused specifically on the functional properties of the PA-800 films in the following sections, i.e., their ferroelectric, energy storage, and electromechanical performance were investigated in more detail. The improved electrical properties in PA-800 films are likely related to the residual stresses in the films, which are reduced most at the highest annealing temperature as shown in Fig. 1c. This is also in agreement with the literature, which demonstrates that annealing at 500 °C leads to enhanced electrical properties compared to both as-deposited films and films annealed at 300 °C [42]. Since a film-substrate interface layer can be observed in PA-800 films, we cannot exclude an influence of this layer on the functional properties of the films.

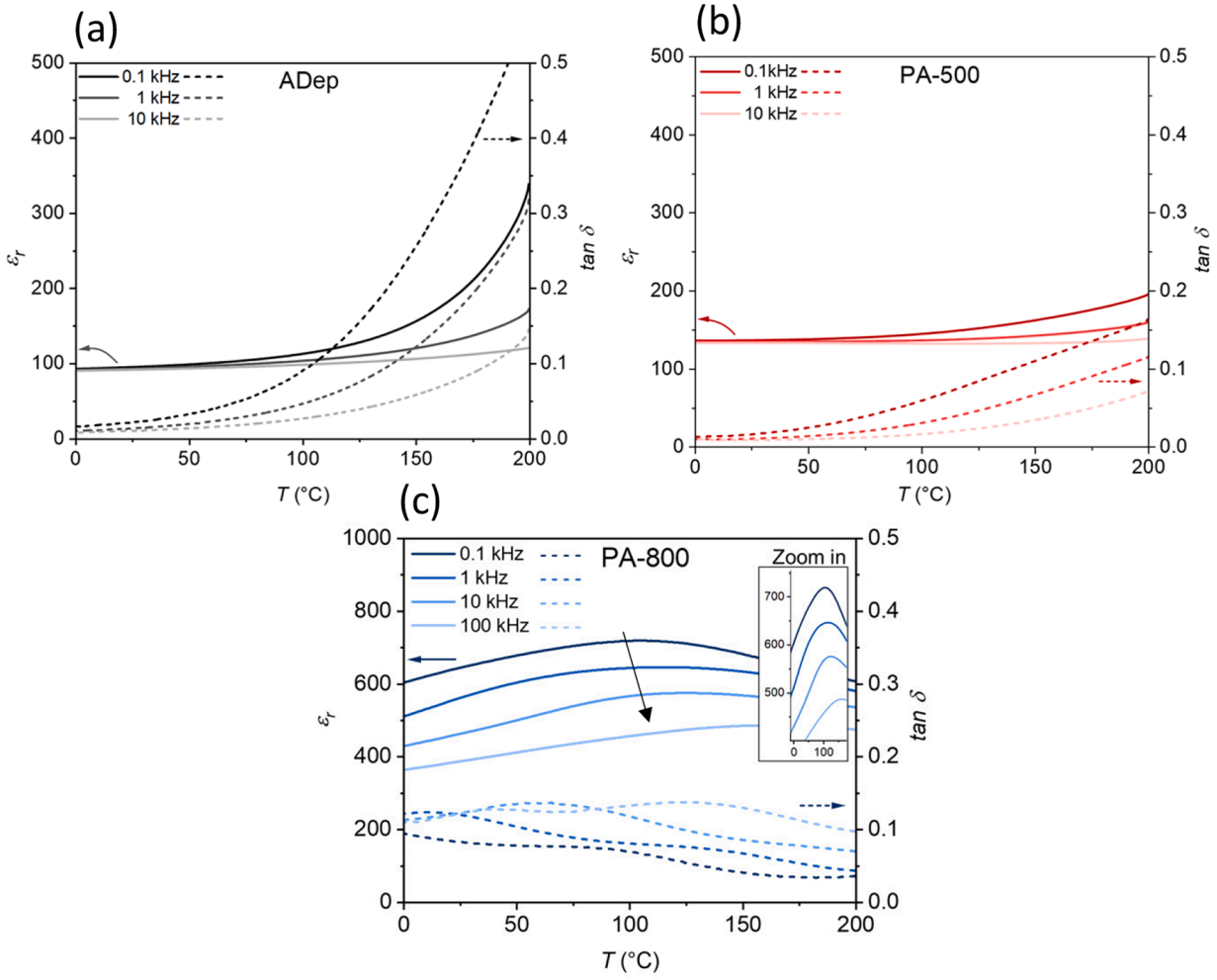

Fig. 5. The ε_r (solid line) and tan δ (dashed line) as a function of temperature for (a) ADep, (b) PA-500 and (c) PA-800 films. The black arrow represents the frequency dependence of the permittivity peaks. For better visualization, a zoomed-in inset is provided. Note the differences in the scale.

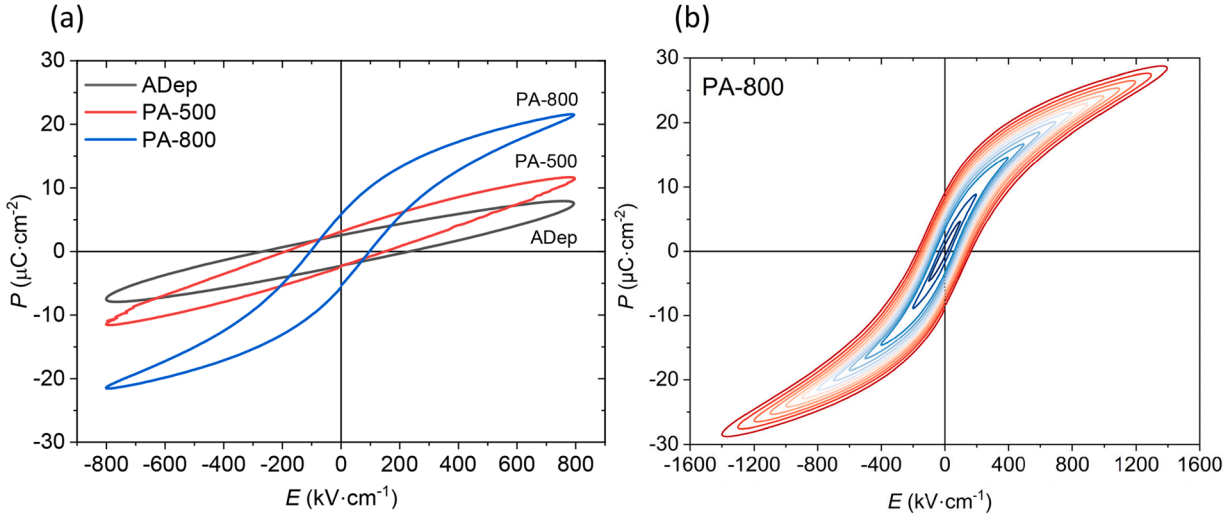

Fig. 6. RT bipolar (a) *P–E* hysteresis loops of ADep, PA-500 and PA-800 films at 800 kV·cm^{-1}. (b) Electric field-dependent bipolar *P–E* hysteresis loops measured up to 1.4 MV·cm^{-1} for PA-800 films.

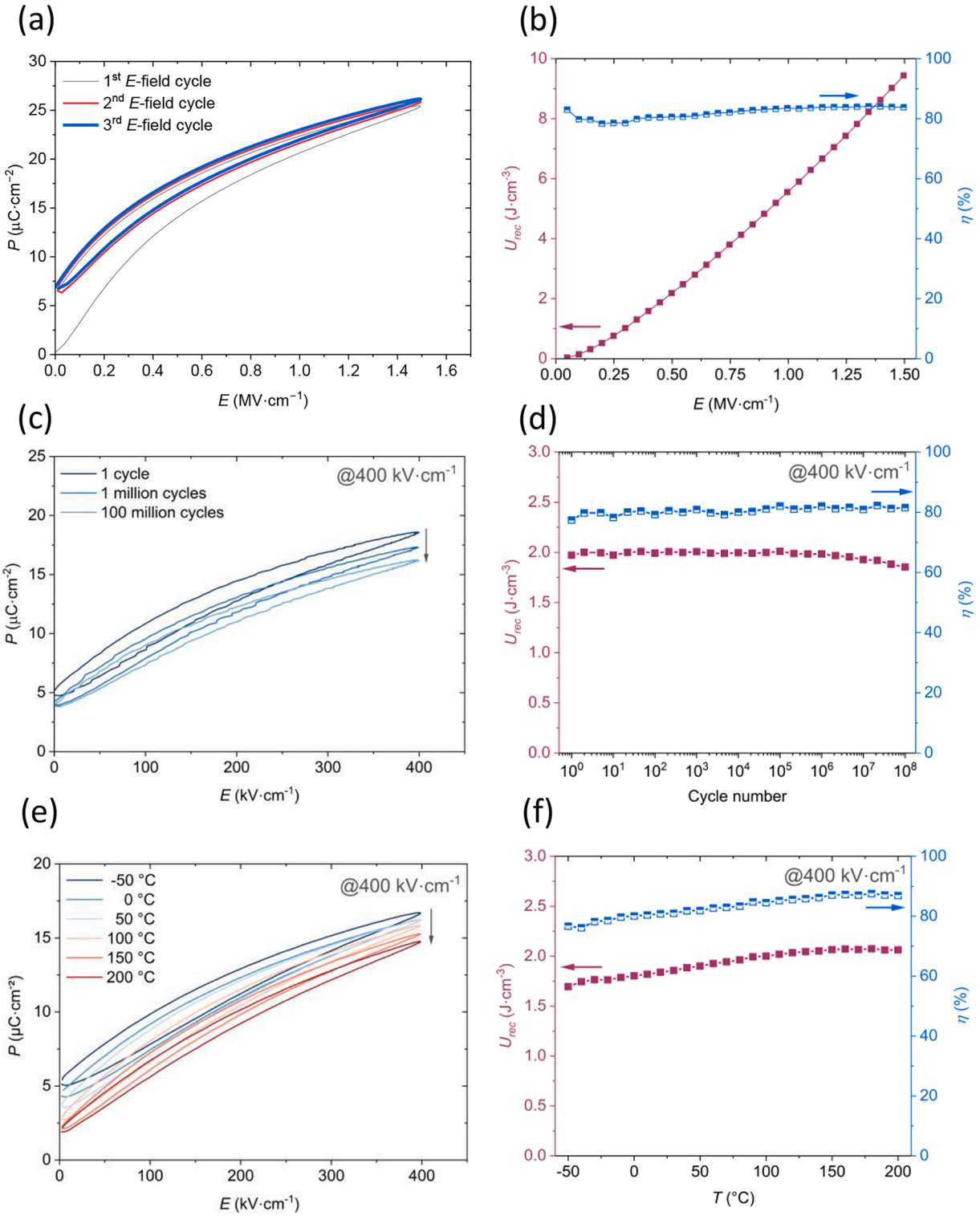

Fig. 7. (a) The first three unipolar *P–E* hysteresis loops of PA-800 films measured at 1.5 MV·cm^{-1} and RT. (c) Electric-field cycling dependence and (e) temperature-dependence of the *P–E* hysteresis loops measured at 400 kV·cm^{-1}. (b, d, f) The corresponding U_{rec} and η properties. The vertical arrows in panels (c) and (e) mark the increase in the number of *E* cycles and temperature from −50 °C to 200 °C, respectively.

The energy storage properties of the PA-800 films were determined based on the recorded unipolar *P–E* hysteresis loops as shown in Fig. 7a. The corresponding energy storage parameters are presented in Fig. 7b. At 1.5 MV·cm^{-1}, U_{rec} and η reach 9.5 J·cm^{-3} and 84 %, respectively. To investigate the applicability of the prepared PA-800 films for energy-storage applications, we investigated the fatigue resistance and temperature stability of the energy-storage performance. First, we tested the fatigue behaviors by recording unipolar *P–E* loops at an electric field of 400 kV·cm^{-1} (Fig. 7c), to evaluate the cycling reliability of the energy storage properties. The sample endured 100 million cycles, during which P_{max} decreases from 18.6 μC·cm^{-2} in the first cycle to 16.2 μC·cm^{-2} in the 100 million cycles (ΔP_{max} = 2.4 μC·cm^{-2}) without

breakdown. Accordingly, U_{rec} decreases from 2.0 J·cm^{-3} to 1.8 J·cm^{-3}, while η increases from 77.4 % to 81.5 % as shown in Fig. 7d. Furthermore, the fatigue stability of the energy storage properties of PA-800 films at 750 kV·cm^{-1} is provided in Supplementary material S8. Secondly, we investigated the thermal-stability of the energy storage performance of PA-800 films by measuring the *P–E* loops at 400 kV·cm^{-1} in the temperature range from −50 °C to 200 °C (Fig. 7e). As the temperature increases from −50 °C to 200 °C, a continuous decrease in polarization and a narrowing of the *P–E* loops are observed. The temperature dependence of the energy storage parameters is shown in Fig. 7f, where the values of U_{rec} and η gradually increase with temperature. The U_{rec} changes from 1.69 J·cm^{-3} to 2.06 J·cm^{-3}, while η changes from 76.6 % to 86.9 %, indicating temperature-stable energy storage properties in the wide temperature range, namely from –50 °C to 200 °C at 400 kV·cm^{-1}. The thermal stability makes them promising for applications in hybrid electric vehicles that require high thermal stability over a broad temperature range of ~ 140 K [81,82].

Since pulsed-power energy-storage systems usually operate under high applied voltages to maximize energy storage, it is important to investigate the DBS of dielectric capacitors [83]. The DBS was evaluated using Weibull analysis and was found to be 1413 kV·cm^{-1}. The results of the Weibull analysis can be seen in Fig. 8. Further details can be found in Supplementary material S9.

For comparison with the literature, Table 1 presents the energy storage properties of our BZT–BCT films with other BZT–BCT-based bulk ceramic, thick films and thin films. The U_{rec} values are in general the highest for thin films, slightly lower for thick films, and the lowest for bulk ceramic samples, as expected and in agreement with the literature [13]. The lower energy storage properties of PA-800 films compared to BZT–BCT-based thin films [23–25] are most likely related to the powder-based thick-film technology, specifically in this case, the aerosol deposition method. Another possible reason for the difference in U_{rec} values is the difference in used electric fields. ref. [23–25] report measurements of BZT–BCT-based thin films at higher electric fields (2000–3500 kV·cm^{-1}) compared to our measurements (1500 kV·cm^{-1}). Nevertheless, the advantage of aerosol deposition is that the process is cost-efficient, easy to perform, and fast, enabling the preparation of many samples within a few minutes. For industrial purposes, this could be beneficial and offset the lower functional performance compared to more time-consuming and expensive thin- and thick-film methods [32,33].

Table 1
Comparison of the energy storage properties of BZT–BCT-based samples prepared in different forms.

Form	Thickness (μm)	U_{rec} (J/cm^3)	η (%)	E (kV/cm)	Ref.
Ceramic[a]	310	0.075	37	25	[84]
Ceramic[a]	-	0.079	87	20	[8]
Ceramic[b]	200	0.274	88	50	[85]
Ceramic[a]	340	0.367	67	60	[86]
Ceramic[c]	-	0.67	83	90	[87]
Ceramic[d]	-	3.71	95	395	[88]
Ceramic[e]	100–120	9.12	95	480	[89]
Thick film (tape casting)[f]	50	2.35	86	410	[90]
Thick film (electrophoretic deposition)[a]	4.3	7.30	75	294	[91]
Thick film (aerosol deposition, free standing)[a]	90	1.34	82	200	[59]
Thick film (aerosol deposition)[a]	6	9.50	84	1500	This work
Thin film (sol-gel)[g]	0.34	46.00	89	3500	[23]
Thin film (sol-gel)[a]	0.20	64.80	73	2000	[24]
Thin film (pulsed laser deposition)[a]	0.36	93.52	43	3470	[25]

[a] : $(Ba_{0.85}Ca_{0.15}Zr_{0.10}Ti_{0.90})O_3$.
[b] : measurements under −160 MPa.
[c] : $0.97(Ba_{0.85}Ca_{0.15}Zr_{0.10}Ti_{0.90})O_3$–$0.03La(Mg_{0.5}Ti_{0.5})O_3$.
[d] : $0.91(Ba_{0.85}Ca_{0.15}Zr_{0.10}Ti_{0.90})O_3$–$0.09Bi_{2/3}(Al_{1/2}Nb_{1/2})O_3$.
[e] : $0.7225Ba_{0.85}Ca_{0.15}Zr_{0.1}Ti_{0.9}O_3$–$0.1275Bi(Zn_{2/3}Ta_{1/3})O_3$–$0.15NaNbO_3$.
[f] : $0.85(Ba_{0.85}Ca_{0.15}Zr_{0.10}Ti_{0.90})O_3$–$0.15Bi(Zn_{0.5}Zr_{0.5})O_3$.
[g] : $Ba_{0.85}Ca_{0.15}Zr_{0.10}Ti_{0.90}O_3$ doped by 1 mol % of Mn.

3.3.3. Macroscopic electromechanical properties

The macroscopic electromechanical properties of the PA-800 films were determined using the aixACCT instrument equipped with a single-beam laser interferometer. For such samples, the electromechanical properties are more suitable to be determined with an instument equipped with a double-beam laser interferometer. Therefore, the single-laser-beam method was first validated by comparing the results obtained with the double-beam interferometer. As shown in Supplementary material S10, the responses using the two methods are comparable. The results obtained with the aixACCT instrument equipped by single-beam laser interferometer at three different *E* are shown in Fig. 9. An *S–E* loops with a maximum of 0.026, 0.044 and 0.052 % were obtained at 220, 300 and 350 kV·cm^{-1}, respectively. The converse effective piezoelectric coefficient values, $d^*_{33\ eff}$ were estimated from the

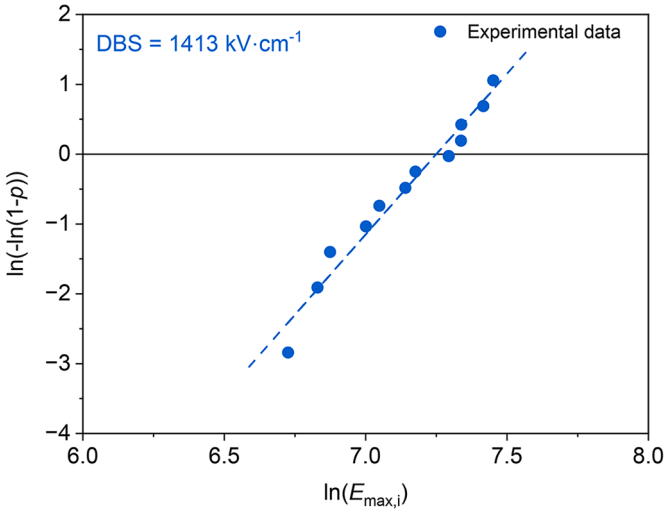

Fig. 8. Weibull distribution analysis of the dielectric breakdown field measurements of the PA-800 films. The dashed blue line represents the linear fit of the measured data points.

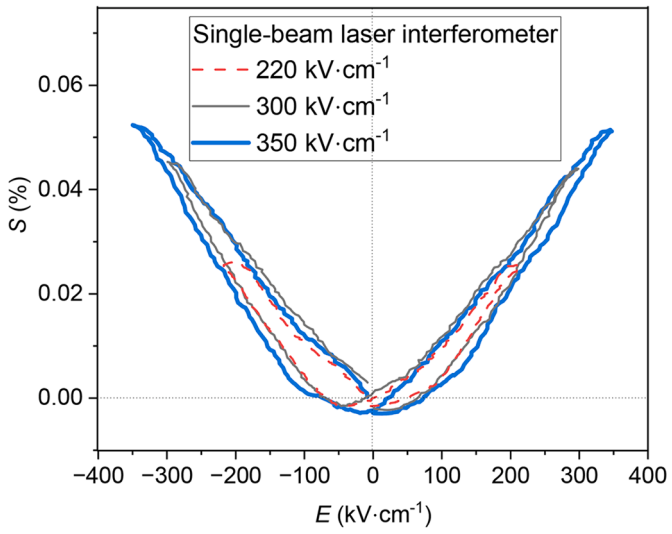

Fig. 9. *S–E* hysteresis loops of PA-800 films measured with a single-beam laser interferometer.

slope of the *S–E* loops by linear regression. The average $d^*_{33\ eff}$ values from right and left side of the loops were found to be 12.4, 15.3 and 15.5 pm·V^{-1} at 220, 300 and 350 kV·cm^{-1}, respectively. The loops present small negative strain, meaning small remanence and thus weak permanent ferroelastic swithing behavior, consistent with the broad temperature-dependent permittvitiy of this sample (Fig. 5c). The small negative strain, the previously shown frequency dispersion of the permittivity peaks (Fig. 5c) as well as slim and tilted *P–E* hysteresis loops (Fig. 7) with low remanence all indicate the relaxor-like behaviour of a PA-800 films.

The literature [7] reports that the piezoelectric response of BZT–BCT bulk ceramics with an average grain size of up to several μm decreases with decreasing grain size. For example, the $d^*_{33\ eff}$ value decreases from 1400 pm·V^{-1} to 190 pm·V^{-1} for the samples with an average grain size of 5 μm and 1 μm, respectively. Since the grain size of the aerosol-deposited films is in the range of tens to hundred of nanometers and assuming a linear relation between grain size and piezoelectric coefficient, in our case $d^*_{33\ eff}$ is expected to be roughly an order of magnitude lower, meaning on the level of tens of pm/V, which is consistent with our results. A similar behavior was observed for PMN–35PT, where the piezoelectric response of the bulk ceramic was 300 pC· N^{-1} [92], while for aerosol-deposited thick films on SS it was ~ 25 pC·N^{-1} [58], which is about ten times lower. While it appears as grain size is crucial, other influences on the reduced electromechanical activity of the films, such as substrate clamping effects or pinning by point defects [93,94] cannot be ruled out.

4. Conclusions

This work demonstrates the successful deposition of dense lead-free BZT–BCT thick films with excellent adhesion onto cost-effective stainless-steel substrates using the aerosol deposition technique. Annealing treatments at 500 °C and 800 °C were employed in order to release the internal residual stresses and further improve the functional properties of the films. The films annealed at 800 °C exhibit a reduced microstrain by 43 % compared to the as-deposited films, a homogeneous piezoelectric behavior over the entire thickness, and promising ferroelectric properties with a well developed polarization–electric field loop, and a high DBS of >1400 kV·cm^{-1}. These films show U_{rec} and η of 9.5 J·cm^{-3} and 84 %, respectively, and demonstrated excellent endurance up to 100 million electric field cycles at 400 kV·cm^{-1} without significant degradation. Furthermore, their energy storage performance remained reliable across a broad temperature range of −50 °C to 200 °C at 400 kV·cm^{-1}. The strain versus electric field measurements showed a maximum strain value of 0.05 % at 350 kV·cm^{-1}, which corresponds to a $d^*_{33\ eff}$ of 15.5 pm·V^{-1}. This relatively low value is most likely due to the fine microstructure, as previously reported for BZT–BCT bulk ceramics [7].

To conclude, lead-free BZT–BCT thick films on a cost-effective stainless-steel substrate demonstrate multifunctional capabilities for energy storage and piezoelectric applications, making them promising candidates for advancing next-generation microelectronic systems. Furthermore, due to their thermal stability, these films are promising for applications in hybrid electric vehicles that require high thermal stability over a broad temperature range.

Data availability

The data that support the findings of this study are available at Zenodo repository [95].

CRediT authorship contribution statement

Soukaina Merselmiz: Writing – review & editing, Writing – original draft, Visualization, Methodology, Investigation, Formal analysis, Data curation, Conceptualization. **Ivana Goričan:** Writing – review & editing, Writing – original draft, Visualization, Validation, Methodology, Investigation, Formal analysis, Data curation, Conceptualization. **Tadej Rojac:** Writing – review & editing, Validation, Methodology, Investigation, Formal analysis, Data curation, Conceptualization. **Vid Bobnar:** Writing – review & editing, Validation, Methodology, Investigation, Data curation. **Victor Regis:** Writing – review & editing, Methodology, Investigation. **Matej Šadl:** Writing – review & editing, Methodology, Investigation. **Val Fišinger:** Writing – review & editing, Investigation, Data curation. **Nejc Suban:** Investigation. **Brigita Kmet:** Writing – review & editing, Methodology, Investigation, Data curation. **Andreja Benčan:** Writing – review & editing, Methodology, Investigation, Data curation. **Andraž Bradeško:** Writing – review & editing, Methodology, Investigation. **Andrej Debevec:** Writing – review & editing, Investigation. **Barbara Malič:** Writing – review & editing, Methodology, Investigation, Funding acquisition, Conceptualization. **Hana Uršič:** Writing – review & editing, Writing – original draft, Supervision, Project administration, Methodology, Investigation, Funding acquisition, Data curation, Conceptualization.

Declaration of competing interest

The authors declare that they have no known competing financial interests or personal relationships that could have appeared to influence the work reported in this paper.

Acknowledgements

This work was supported by the Slovenian Research and Innovation Agency (research project J2–60035, J2–3058, N2–0212, research core funding P2–0105 and Young Researcher project). The technical assistance of Silvo Drnovšek, Jena Cilenšek and Fran Zupet is greatly acknowledged.

Supplementary materials

Supplementary material associated with this article can be found, in the online version, at doi:10.1016/j.actamat.2025.121749.

References

[1] European Union, Directive 2002/95/EC restriction of the use of certain hazardous substances in electrical and electronic equipment (RoHS), Official. J. Eur. Union 46 (L37) (2003) 19–23.
[2] The marking for presence of the specific chemical substances for electrical and electronic equipment, *Japanese Standards Association*, JIS C 0950 (2005).
[3] K. Reczek, L.M. Benson, A guide to United States apparel and household textiles compliance requirements, *NIST Interagency/Internal Report (NaISTIR)* (2013).
[4] W. Liu, X. Ren, Large piezoelectric effect in Pb-free ceramics, Phys. Rev. Lett. 103 (2009) 257602.
[5] I. Coondoo, N. Panwar, H. Amorín, V.E. Ramana, M. Alguerõ, A. Kholkin, Enhanced piezoelectric properties of praseodymium-modified lead-free $(Ba_{0.85}Ca_{0.15})(Ti_{0.90}Zr_{0.10})O_3$ Ceramics, J. Am. Ceram. Soc. 98 (2015) 3127–3135.
[6] I. Coondoo, N. Panwar, H. Amorín, A.L. Kholkin, Synthesis and characterization of lead-free $0.5Ba(Zr_{0.2}Ti_{0.8})O_3$–$0.5(Ba_{0.7}Ca_{0.3})TiO_3$ ceramic, J. Appl. Phys. 113 (2013) 214107, 1–6.
[7] H. Amorín, M. Venet, J.E. García, D.A. Ochoa, P. Ramos, J. López-Sánchez, J. Rubio-Zuazo, A. Castro, M. Algueró, Insights into the early size effects of lead-free piezoelectric $Ba_{0.85}Ca_{0.15}Zr_{0.1}Ti_{0.9}O_3$, Adv. Electron. Mater. 10 (2024) 2300556, 1–12.
[8] W. Cai, Q. Zhang, C. Zhou, R. Gao, S. Zhang, Z. Li, R. Cu, G. Chen, X. Deng, Z. Wang, C. Fu, Synergistic effect of grain size and phase boundary on energy storage performance and electric properties of BCZT ceramics, J. Mater. Sci.: Mater. Electron. 31 (2020) 9167–9175.
[9] S. López-Blanco, D.A. Ochoa, H. Amorín, A. Castro, M. Algueró, J.E. García, Fine-grained high-performance $Ba_{0.85}Ca_{0.15}Zr_{0.1}Ti_{0.9}O_3$ piezoceramics obtained by current-controlled flash sintering of nanopowders, J. Eur. Ceram. Soc. 43 (2023) 7440–7445.
[10] D.S. Keeble, F. Benabdallah, P.A. Thomas, M. Maglione, J. Kreisel, Revised structural phase diagram of $(Ba_{0.7}Ca_{0.3}TiO_3)$–$(BaZr_{0.2}Ti_{0.8}O_3)$, Appl. Phys. Lett. 102 (2013) 092903.

[11] M. Acosta, N. Novak, W. Jo, J. Rödel, Relationship between electromechanical properties and phase diagram in the $Ba(Zr_{0.2}Ti_{0.8})O_3$–$x(Ba_{0.7}Ca_{0.3})TiO_3$ lead-free piezoceramic, Acta Mater 80 (2014) 48–55.

[12] A.R. Jayakrishnan, J.P.B. Silva, K. Kamakshi, D. Dastan, V. Annapureddy, M. Pereira, K.C. Sekhar, Are lead-free relaxor ferroelectric materials the most promising candidates for energy storage capacitors? Prog. Mater. Sci. 132 (2023) 101046.

[13] H. Palneedi, M. Peddigari, G.T. Hwang, D.Y. Jeong, J. Ryu, High-performance dielectric ceramic films for energy storage capacitors: progress and outlook, Adv. Funct. Mater. 28 (2018) 1803665.

[14] G. Wang, Z. Lu, Y. Li, L. Li, H. Ji, A. Feteira, D. Zhou, D. Wang, S. Zhang, I. M. Reaney, Electroceramics for high-energy density capacitors: current status and future perspectives, Chem. Rev. 121 (2021) 6124–6172.

[15] X. Kong, L. Yang, F. Meng, T. Zhang, H. Zhang, Y.H. Lin, H. Huang, S. Zhang, J. Guo, C.W. Nan, High-entropy engineered $BaTiO_3$-based ceramic capacitors with greatly enhanced high-temperature energy storage performance, Nat. Commun. 16 (2025) 885, 1–9.

[16] L. Chen, C. Zhou, L. Zhu, H. Qi, J. Chen, Compromise optimized superior energy storage performance in lead-free antiferroelectrics by antiferroelectricity modulation and nanodomain engineering, Small 20 (2023) 2306486, 1–8.

[17] H. Qi, R. Zuo, A. Xie, A. Tian, J. Fu, Y. Zhang, S. Zhang, Ultrahigh energy-storage density in $NaNbO_3$-based lead-free relaxor antiferroelectric ceramics with nanoscale domains, Adv. Funct. Mater. 29 (2019) 1923877, 1–8.

[18] A. Xie, J. Fu, R. Zuo, X. Jiang, T. Li, Z. Fu, Y. Yin, X. Li, S. Zhang, Supercritical relaxor nanograined ferroelectrics for ultrahigh-energy-storage capacitors, Adv. Mater. 34 (2022) 2204356, 1–9.

[19] Q. Chai, Z. Liu, Z. Deng, Z. Peng, X. Chao, J. Lu, H. Huang, S. Zhang, Z. Yang, Excellent energy storage properties in lead-free ferroelectric ceramics via heterogeneous structure design, Nat. Commun. 16 (2025) 1633, 1–9.

[20] W. Cao, R. Lin, X. Hou, L. Li, F. Li, D. Bo, B. Ge, D. Song, J. Zhang, Z. Cheng, C. Wang, Interfacial polarization restriction for ultrahigh energy-storage density in lead-free ceramics, Adv. Funct. Mater. 33 (2023) 2301027, 1–11.

[21] J. Fu, A. Xie, R. Zuo, Y. Liu, H. Qi, Z. Wang, Q. Feng, J. Guo, K. Zeng, X. Chen, Z. Fu, Y. Zhang, X. Jiang, T. Li, S. Zhang, Y.A. Lin, C.W. Nan, A highly polarizable concentrated dipole glass for ultrahigh energy storage, Nat. Commun. 15 (2024) 7338, 1–10.

[22] J. Jiang, X. Meng, L. Li, S. Guo, M. Huang, J. Zhang, J. Wang, X. Hao, H. Zhu, S. T. Zhang, Ultrahigh energy storage density in lead-free relaxor antiferroelectric ceramics via domain engineering, Energy Storage Mater 43 (2021) 383–390.

[23] S.W. Konsago, K. Ziberna, A. Matavz, B. Mandal, S. Glinsek, G.L. Brennecka, H. Ursic, B. Malic, High energy storage density and efficiency of $0.5Ba(Zr_{0.2}Ti_{0.8})O_3$–$0.5(Ba_{0.7}Ca_{0.3})TiO_3$ thin films on platinized sapphire substrates, J. Mater. Chem. A. Mater. 13 (2024) 2911–2919.

[24] S.R. Reddy, V.V.B. Prasad, S. Bysakh, V. Shanker, N. Hebalkar, S.K. Roy, Superior energy storage performance and fatigue resistance in ferroelectric BCZT thin films grown in an oxygen-rich atmosphere, J. Mater. Chem. C. Mater. 7 (2019) 7073–7082.

[25] V.S. Puli, D.K. Pradhan, I. Coondoo, N. Panwar, S. Adireddy, S. Luo, R.S. Katiyar, D. B. Chrisey, Observation of large enhancement in energy-storage properties of lead-free polycrystalline $0.5BaZr_{0.2}Ti_{0.8}O_3$–$0.5Ba_{0.7}Ca_{0.3}TiO_3$ ferroelectric thin films, J. Phys. D. Appl. Phys. 52 (2019) 255304, 1–10.

[26] M. Ohring, The Materials Science of Thin Films, Academic Press, United Stated of America, 1992.

[27] L.B. Freund, S. Suresh, Thin Film Materials: Stress, Defect Formation and Surface Evolution, Cambridge University Press, United Kingdom, 2004.

[28] R.A. Dorey, Ceramic Thick Films For MEMS and Microdevices, Elsevier, United Kingdom, 2012.

[29] B. Malic, D. Kuscer, M. Vrabelj, J. Koruza, Review of methods for powder-based processing, in: G. Korotcenkov (Ed.), Chapter 5 in the Book Magnetic, ferroelectric, and Multiferroic Metal Oxides, Elsevier, 2018.

[30] M. Kosec, D. Kuscer, J. Holc, in: L. Pardo, J. Ricote (Eds.), Processing of Ferroelectric Ceramic Thick films, Chapter 2 in the Book Multifunctional polycrystalline Ferroelectric Materials – Processing and Properties, Springer, 2011.

[31] F. Fu, B. Shen, Z. Xu, J. Zhai, Electric properties of $BaTiO_3$ lead-free textured piezoelectric thick film by screen printing method, J. Electroceramics 33 (2014) 208–213.

[32] D. Hanft, J. Exner, M. Schubert, T. Stöcker, P. Fuierer, R. Moos, An overview of the aerosol deposition method: process fundamentals and new trends in materials applications, J. Ceram. Sci. Technol. 6 (2015) 147–181.

[33] J. Akedo, Room temperature impact consolidation (RTIC) of fine ceramic powder by aerosol deposition method and applications to microdevices, J. Therm. Spray Technol. 17 (2008) 181–198.

[34] M. Sadl, O. Condurache, A. Bencan, M. Dragomir, U. Prah, B. Malic, M. Deluca, U. Eckstein, D. Hausmann, N.H. Khansur, K.G. Webber, H. Ursic, Energy-storage-efficient $0.9Pb(Mg_{1/3}Nb_{2/3})O_3$–$0.1PbTiO_3$ thick films integrated directly onto stainless steel, Acta. Mater. 221 (2021) 117403, 1–11.

[35] M. Sadl, A. Lebar, J. Valentincic, H. Ursic, Flexible energy-storage ceramic thick-film structures with high flexural fatigue endurance, ACS Appl. Energy Mater. 5 (2022) 6896–6902.

[36] B. Velkavrh, U. Tomc, M. Sadl, V. Regis, M. Koblar, B. Colaric, A. Kitanovski, H. Ursic, Preparation of dielectric layers for applications in digital microfluidic thermal switches, Inf. MIDEM 54 (2024) 1–8.

[37] J. Akedo, M. Lebedev, Microstructure and electrical properties of lead zirconate titanate ($Pb(Zr_{52}/Ti_{48})O_3$) thick films deposited by aerosol deposition method, Japanese J. Appl. Physics 38 (1999) 5397–5401.

[38] A. Chrir, O. Rojas, M. Bavencoffe, F. Rubio-Marcos, J. López-Sánchez, L. Boyer, O. Durand-Panteix, P. Marchet, Elaboration, post-annealing and energy harvesting performance of NBT–6BT thick films produced by aerosol deposition, J. Eur. Ceram. Soc. 45 (2025) 117559, 1–13.

[39] B. Xie, C. Jiang, Y. Li, I. Cotton, D.A. Hall, Aerosol deposition of alumina ceramic coatings on polyether ether ketone (PEEK) for high-voltage insulation, J. Mater. Res. Tehnol. 38 (2025) 4688–4697.

[40] N.H. Khansur, U. Eckstein, L. Benker, U. Deisinger, B. Merle, K.G. Webber, Room temperature deposition of functional ceramic films on low-cost metal substrate, Ceram. Int. 44 (2018) 16295–16301.

[41] M. Schubert, J. Exner, R. Moos, Influence of carrier gas composition on the stress of Al_2O_3 coatings prepared by the aerosol deposition method, Materials (Basel) 7 (2014) 5633–5642.

[42] N.H. Khansur, U. Eckstein, K. Riess, A. Martin, J. Drnec, U. Deisinger, K.G. Webber, Synchrotron X-ray microdiffraction study of residual stresses in $BaTiO_3$ films deposited at room temperature by aerosol deposition, Scr. Mater. 157 (2018) 86–89.

[43] J. Akedo, Aerosol deposition of ceramic thick films at room temperature: densification mechanism of ceramic layers, J. Am. Ceram. Soc. 89 (2006) 1834–1839.

[44] J. Adamczyk, P. Fuierer, Compressive stress in nano-crystalline titanium dioxide films by aerosol deposition, Surf. Coatings Technol. 350 (2018) 542–549.

[45] J. Exner, T. Nazarenus, D. Hanft, J. Kita, R. Moos, What happens during thermal post-treatment of powder aerosol deposited functional ceramic films? Explanations based on an experiment-enhanced literature survey, Adv. Mater. 32 (2020) 1908104.

[46] M. Sadl, U. Prah, V. Kovacova, E. Defay, T. Rojac, A. Lebar, J. Valentincic, H. Ursic, Multifunctional flexible ferroelectric thick-film structures with energy storage, piezoelectric and electrocaloric performance, J. Mater. Chem. C 11 (2023) 10058–10068.

[47] T. Hoshina, T. Furuta, Y. Kigoshi, S. Hatta, N. Horiuchi, H. Takeda, T. Tsurumi, Size effect of nanograined $BaTiO_3$ ceramics fabricated by aerosol deposition method, Jpn. J. Appl. Phys. 49 (2010) 09MC02.

[48] K. Žiberna, M. Šadl, A. Drnovšek, G. Dražić, H. Uršič, A. Benčan, Influence of thermal treatment on the cross-sectional properties of aerosol-deposited $Pb(Mg_{1/3}Nb_{2/3})O_3$−$PbTiO_3$ thick films, Crystals 13 (2023) 536, 1–10.

[49] Q. Zou, H.E. Ruda, B.G. Yacobi, K. Saegusa, M. Farrell, Dielectric properties of lead zirconate titanate thin films deposited on metal foils, Appl. Phys. Lett. 77 (2000) 1038–1040.

[50] N.R. Baddoo, Stainless steel in construction: a review of research, applications, challenges and opportunities, J. Constr. Steel. Res. 64 (2008) 1199–1206.

[51] L. Gardner, The use of stainless steel in structures, Prog. Struct. Eng. Mater. 7 (2005) 45–55.

[52] G. Gedge, Structural uses of stainless steel - buildings and civil engineering, J. Constr. Steel Res. 64 (2008) 1194–1198.

[53] AZO Materials, Medical applications of stainless steel 304 (UNS S30400), (2012) https://www.azom.com/article.aspx?ArticleID=6641 (last accessed October, 2025).

[54] Y. Kawakami, H. Yoshikawa, K. Komagata, J. Akedo, Powder preparation for $0.5Pb(Ni_{1/3}Nb_{2/3})O_3$–$0.15PbZrO_3$–$0.35PbTiO_3$ thick films by the aerosol deposition method, J. Cryst. Growth. 275 (2005) e1295–e1300.

[55] Y. Kawakami, M. Watanabe, K.I. Arai, S. Sugimoto, Effects of substrate materials on piezoelectric properties of $BaTiO_3$ thick films deposited by aerosol deposition, Jpn. J. Appl. Phys. 55 (2016) 10TA10, 1–5.

[56] S.W. Oh, J. Akedo, J.H. Park, Y. Kawakami, Fabrication and evaluation of lead-free piezoelectric ceramic LF4 thick film deposited by aerosol deposition method, Jpn. J. Appl. Phys., Part 1 45 (2006) 7465–7470.

[57] J. Akedo, M. Lebedev, Effects of annealing and poling conditions on piezoelectric properties of $Pb(Zr_{0.52}Ti_{0.48})O_3$ thick films formed by aerosol deposition method, J. Cryst. Growth. 235 (2002) 415–420.

[58] M. Sadl, K. Nadaud, M. Bah, F. Levassort, U. Eckstein, N.H. Khansur, K.G. Webber, H. Ursic, Multifunctional energy storage and piezoelectric properties of $0.65Pb(Mg_{1/3}Nb_{2/3})O_3$–$0.35PbTiO_3$ thick films on stainless-steel substrates, JPhys. Energy. 4 (2022) 024004, 1–9.

[59] J.G. Maier, T. Fuggerer, D. Urushihara, A. Martin, N.H. Khansur, K.I. Kakimoto, K. G. Webber, The impact of grain growth on the functional properties in room-temperature powder aerosol deposited free-standing $(Ba,Ca)(Zr,Ti)O_3$ thick films, Crystals 14 (2024) 296, 1–16.

[60] Y. Kawakami, M. Watanabe, K.-I. Arai, S. Sugimoto, Piezoelectric properties and microstructure of $BaTiO_3$ films on heat-resistant stainless-steel substrates deposited using aerosol deposition, Trans. Mater. Res. Soc. Japan. 41 (2016) 279–283.

[61] F. Zhuo, U.R. Eckstein, N.H. Khansur, C. Dietz, D. Urushihara, T. Asaka, K. Kakimoto, K.G. Webber, X. Fang, J. Rödel, Temperature-induced changes of the electrical and mechanical properties of aerosol-deposited $BaTiO_3$ thick films for energy storage applications, J. Am. Ceram. Soc. 105 (2022) 4108–4121.

[62] M. Bentzen, J. Maier, U. Eckstein, J. He, A. Henss, N. Khansur, J. Glaum, Enhanced grain growth and dielectric properties in aerosol deposited $BaTiO_3$, J. Eur. Ceram. Soc. 43 (2023) 4386–4394.

[63] J.G. Maier, M. Kuhfuß, D. Urushihara, A. Gadelmawla, N.H. Khansur, D. Hall, M. Algueró, A. Martin, K. Kakimoto, K.G. Webber, Influence of grain size on electromechanical properties of $(Ba,Ca)(Zr,Ti)O_3$: a multiscale analysis using spark plasma sintering and aerosol deposition, Ceram. Int. 50 (2024) 26780–26791.

[64] M. Sadl, U. Tomc, U. Prah, H. Ursic, Protective alumina coatings prepared by aerosol deposition on magnetocaloric gadolinium elements, Inf. MIDEM 49 (2019) 177–182.

[65] J. Rodríguez-Carvajal, Recent advances in magnetic structure determination by neutron powder diffraction, Phys. B Phys. Condens. Matter 192 (1993) 55–69.
[66] G.K. Williamson, W.H. Hall, X-ray line broadening from filed aluminium and wolfram, Acta Metall 1 (1953) 22–31.
[67] A. Khorsand Zak, W.H. Abd. Majid, M.E. Abrishami, R. Yousefi, X-ray analysis of ZnO nanoparticles by Williamson-Hall and size-strain plot methods, Solid State Sci. 13 (2011) 251–256.
[68] H. Ursic, M. Sadl, Investigation of piezoelectric 0.65Pb($Mg_{1/3}Nb_{2/3}$)O_3–0.35$PbTiO_3$ films in cross section using piezo-response force microscopy, Appl. Phys. Lett. 121 (2022) 296.
[69] H. Ursic, U. Prah, Investigations of ferroelectric polycrystalline bulks and thick films using piezoresponse force microscopy, Proc. R. Soc. A Math. Phys. Eng. Sci. 475 (2019) 20180782.
[70] W. Cai, Q. Zhang, C. Zhou, R. Gao, F. Wang, G. Chen, X. Deng, Z. Wang, N. Deng, L. Cheng, C. Fu, Effects of oxygen partial pressure on the electrical properties and phase transitions in (Ba,Ca)(Ti,Zr)O_3 ceramics, J. Mater. Sci. 55 (2020) 9972–9992.
[71] V.D. Dolzhenko, A.V. Avdei, E.G. Evtushenko, V.A. Mukhanov, P.N. Komozin, Yu. M. Kiselev, Matrix" stabilization of RhVI ions in the structure of MIIEVIO4 (E = Cr, Mo, W), Doklady Chem. 379 (2001) 209–211.
[72] S.W. Konsago, A. Debevec, J. Cilensek, B. Kmet, B. Malic, Linear thermal expansion of 0.5Ba($Zr_{0.2}Ti_{0.8}$)O_3–0.5($Ba_{0.7}Ca_{0.3}$)TiO_3 Bulk Ceramic, Inf. MIDEM 53 (2023) 233–238.
[73] AZO Materials, Stainless Steel - Grade 304 (UNS S30400). https://www.azom.com/properties.aspx?ArticleID=965 (last accessed June 2025).
[74] Y. Il Kim, J.K. Jung, K.S. Ryu, Structural study of nano $BaTiO_3$ powder by Rietveld refinement, Mater. Res. Bull. 39 (2004) 1045–1053.
[75] X. Liu, R.C. Liebermann, X-ray powder diffraction study of $CaTiO_3$ perovskite at high temperatures, Phys. Chem. Miner. 20 (1993) 171–175.
[76] X. Lu, J. Zhu, Z. Liu, X. Xu, Y. Wang, Phase transition related stress in ferroelectric thin films, Thin Solid Films 375 (2000) 15–18.
[77] J. Hao, W. Bai, W. Li, J. Zhai, Correlation between the microstructure and electrical properties in high-performance ($Ba_{0.85}Ca_{0.15}$)($Zr_{0.1}Ti_{0.9}$)O_3 lead-free piezoelectric ceramics, J. Am. Ceram. Soc. 95 (2012) 1998–2006.
[78] U. Prah, M. Sadl, A. Torello, P. Lheritier, V. Kovacova, H. Ursic, E. Defay, Direct electrocaloric characterization of ceramic films, Small Methods 7 (2023) 2300212, 1–8.
[79] M. Suzuki, J. Akedo, Temperature dependence of dielectric properties of barium titanate ceramic films prepared by aerosol deposition method, Jpn. J. Appl. Phys. 49 (2010) 09MA10, 1–5.
[80] U. Eckstein, J. Exner, A. Bencan Golob, K. Ziberna, G. Drazic, H. Ursic, H. Wittkämper, C. Papp, J. Kita, R. Moos, K.G. Webber, N.H. Khansur, Temperature-dependent dielectric anomalies in powder aerosol deposited ferroelectric ceramic films, J. Mater. 8 (2022) 1239–1250.
[81] Q. Li, L. Chen, M.R. Gadinski, S. Zhang, G. Zhang, H. Li, A. Haque, L.Q. Chen, T. Jackson, Q. Wang, Flexible high-temperature dielectric materials from polymer nanocomposites, Nature 523 (2015) 576–579.
[82] C. Yang, J. Qian, P. Lv, H. Wu, X. Lin, K. Wang, J. Ouyang, S. Huang, X. Cheng, Z. Cheng, Flexible lead-free BFO-based dielectric capacitor with large energy density, superior thermal stability, and reliable bending endurance, J. Mater. 6 (2020) 200–208.
[83] M.D. Nguyen, Y.A. Birkhölzer, E.P. Houwman, G. Koster, G. Rijnders, Enhancing the energy-storage density and breakdown strength in $PbZrO_3$/$Pb_{0.9}La_{0.1}Zr_{0.52}Ti_{0.48}O_3$-derived antiferroelectric/relaxor-ferroelectric multilayers, Adv. Energy Mater. 12 (2022) 2200517.
[84] S. Merselmiz, Z. Hanani, D. Mezzane, A.G. Razumnaya, M. Amjoud, L. Hajji, S. Terenchuk, B. Rozic, I.A. Luk'yanchuk, Z. Kutnjak, Thermal-stability of the enhanced piezoelectric, energy storage and electrocaloric properties of a lead-free BCZT ceramic, RSC Adv 11 (2021) 9459–9468.
[85] J.G. Maier, A. Gadelmawla, N.H. Khansur, K.G. Webber, Stress-induced tailoring of energy storage properties in lead-free $Ba_{0.85}Ca_{0.15}Zr_{0.1}Ti_{0.9}O_3$ ferroelectric bulk ceramics, J. Materiomics 9 (2023) 673–682.
[86] Z. Hanani, S. Merselmiz, D. Mezzane, M. Amjoud, A. Bradesko, B. Rozic, M. Lahcini, M. El Marssi, A.V. Ragulya, I.A. Luk'Yanchuk, Z. Kutnjak, M. Gouné, Thermally-stable high energy storage performances and large electrocaloric effect over a broad temperature span in lead-free BCZT ceramic, RSC Adv. 10 (2020) 30746–30755.
[87] J.H. Li, X.N. Shi, Y.H. Zhang, J.Y. Li, D.H. Shao, T.K. Liang, S.Q. Wang, Z.Y. Yang, Y. Chen, Y.F. Wang, F. Yang, Effect of LMT doping on microstructure and electrical properties of BCZT ceramics, Ceram. Int. 51 (2025) 12577–12586.
[88] S. Dang, Y. Sun, Z. Peng, T. Yang, Y. Wang, Q. Chai, D. Wu, P. Liang, L. Wei, X. Chao, Z. Yang, Simultaneous achievement of high energy storage density and ultrahigh efficiency in BCZT-based relaxor ceramics at moderate electric field, J. Power Sources 627 (2025) 235846, 1–9.
[89] L. Diwu, P. Wang, T. Wang, Q. Zhu, J. Luo, Y. Liu, P. Gao, Y. TIan, H. Jing, X. Ren, Z. Wang, Z. Sun, Engineering ordered-disordered domains for high-performance energy storage in BCZT-based relaxor ferroelectrics, Small 21 (2025) 2503713, 1–13.
[90] X. Yang, B. Fang, X. Lu, S. Zhang, J. Ding, Improving energy storage properties of ($Ba_{0.85}Ca_{0.15}$($Zr_{0.1}Ti_{0.9}$)O_3 lead-free ceramic thick films by doping Bi($Zn_{0.5}Zr_{0.5}$)O_3, Appl. Phys. 131 (2025) 703, 1–17.
[91] E.V. Ramana, N.V. Prasad, N.M. Ferreira, A. Mahajan, I. Bdikin, M.A. Valente, F. A. Essa, B. Saleh, Insights into improved ferroelectric and electrocaloric performance of $Ba_{0.85}Ca_{0.15}Ti_{0.9}Zr_{0.1}O_3$ thick films grown by the electrophoretic deposition, Surf. Interfaces 33 (2022) 102257, 1–13.
[92] M. Algueró, J. Ricote, R. Jiménez, P. Ramos, J. Carreaud, B. Dkhil, J.M. Kiat, J. Holc, M. Kosec, Size effect in morphotropic phase boundary Pb($Mg_{1/3}Nb_{2/3}$)O_3–$PbTiO_3$, Appl. Phys. Lett. 91 (2007) 112905, 1–3.
[93] F. Xu, S. Trolier-McKinstry, W. Ren, B. Xu, Z.-L. Xie, K.J. Hemker, Domain wall motion and its contribution to the dielectric and piezoelectric properties of lead zirconate titanate films, J. Appl. Phys. 89 (2001) 1336–1348.
[94] F. Griggio, S. Jesse, A. Kumar, O. Ovchinnikov, H. Kim, T.N. Jackson, D. Damjanovic, S.V. Kalinin, S. Trolier-McKinstry, Substrate clamping effects on irreversible domain wall dynamics in lead zirconate titanate thin films, Phys. Rev. Lett. 108 (2012) 157604, 1–5.
[95] I. Goričan, H. Uršič, Capacitive energy-storage and electromechanical properties of aerosol-deposited 0.5$BaZr_{0.2}Ti_{0.8}O_3$–0.5$Ba_{0.7}Ca_{0.3}TiO_3$ films, Zenodo (2025), https://doi.org/10.5281/zenodo.15773335.